Anthropogenic impacts on recent decadal change in temperature extremes over China: relative roles of greenhouse gases and anthropogenic aerosols

Article

Accepted Version

Anthropogenic impacts on recent decadal change in temperature extremes over China: relative roles of greenhouse gases and anthropogenic aerosols

Wei Chen[1] and Buwen Dong[2]

[1.] State Key Laboratory of Numerical Modeling for Atmospheric Sciences and Geophysical Fluid Dynamics, Institute of Atmospheric Physics, Chinese Academy of Sciences, Beijing 100029

[2.] National Centre for Atmospheric Science-Climate, Department of Meteorology, University of Reading, Reading, UK

Corresponding author:

Wei Chen,

Institute of Atmospheric Physics,

Chinese Academy of Sciences,

P. O. Box 9804, Beijing 100029, China.

E-mail: chenwei@mail.iap.ac.cn

Abstract

Observational analysis indicates significant changes in some temperature extremes over China across the mid-1990s. The decadal changes in hot extremes are characterized as a rise in annual hottest day and night temperatures (TXx and TNx) and an increase in frequencies of summer days (SU) and tropical night (TR). The decadal changes in cold extremes are distinguished by a rise in annual coldest day and night temperatures (TXn and TNn) and a decrease in frequencies of ice days (ID) and frost days (FD). These decadal changes manifest not only over China as a whole, but also over individual climate sub-regions.

An atmosphere-ocean-mixed-layer coupled model forced by changes in greenhouse gases (GHG) concentrations and anthropogenic aerosol (AA) emissions realistically reproduces the general spatial patterns and magnitudes of observed changes in both hot and cold extremes across the mid-1990s, suggesting a pronounced role of anthropogenic changes in these observed decadal changes. Separately, changes in GHG forcing lead to rise in TXx, TNx, TXn and TNn, increase in frequencies of SU and TR and decrease in frequencies of ID and FD over China through increased Greenhouse Effect with positive clear sky longwave radiation and play a dominant role in simulated changes of both hot and cold extremes over China. The AA forcing changes tend to cool Southern China and warm Northern China during summer via aerosol-radiation interaction and AA-induced atmosphere-cloud feedback and therefore lead to some weak increase in hot extremes over Northern China and decrease over Southeast China.

Meanwhile, AA changes lead to warming over China during winter through cloud feedbacks related to aerosol induced cooling over tropical Indian Ocean and western tropical Pacific, and also induce changes in cold extremes the same sign as those induced by GHG, but with weak magnitude.

Key words: hot temperature extremes; cold temperature extremes; China; decadal change; the mid-1990s; greenhouse gases; anthropogenic aerosol

1. Introduction

Understanding of the changes in climate extremes and the underling drivers is important for human society, economies and ecosystems. In the last few decades, temperature extremes exhibited robust changes at global and regional scales, with more hot extremes and less cold extremes (e.g., Alexander et al. 2006; Donat et al. 2013). The impacts of temperature extremes have highlighted the urgency of improved understanding of their physical causes and to what extent they are manifested in a warming world (e.g., Otto et al. 2012; Christidis et al. 2013; Perkins 2015).

China experienced record-breaking heat waves and temperature extremes that imposed disastrous impacts on individuals and society (e.g., Yin et al. 2016; Zhou et al. 2016; Freychet et al. 2017). Such as the 2013 heat wave in Central and Eastern China (Ma et al. 2017), the 2014 hot and dry summer over Northeast China (Wilcox et al. 2015) and the 2015 extreme hot summer over Western China (Sun et al. 2016). The trend of continuous warming and increase in hot extremes over China might be

42 associated with the global-scale warming (e.g., Wei et al. 2011). This warming trend
43 and increase in hot temperature extremes can be reproduced by the future climate
44 change scenario (Yao et al. 2012), implying the role of anthropogenic activity in
45 increasing hot temperature extremes.

46 Previous attribution studies detected that anthropogenic activity, as a combined
47 effects of greenhouse gases (GHG) concentrations and anthropogenic aerosol (AA)
48 emissions, induces the changes in temperature extremes over China. Approximately 90%
49 of the observed changes in hot extremes since mid-20th century may contributed by
50 anthropogenic forcing (e.g., Wen et al. 2013; Yin et al. 2016). The summer mean
51 temperature and temperature extremes in Eastern China can be increased by the
52 anthropogenic influence (Sun et al. 2014). The direct impacts of changes in GHG
53 concentrations and AA contribute to the 2014 hot and dry summer in Northeast China,
54 beside SST anomaly (Wilcox et al. 2015). Both anthropogenic factors and atmospheric
55 natural variability contributed to the 2013 mid-summer heat wave in Central and
56 Eastern China (Ma et al. 2017).

57 Physically, the climate system warms in response to the increase in GHG
58 concentrations, because the atmosphere traps more outgoing longwave radiation (e.g.,
59 Cubasch et al. 2001; Dong et al. 2009, 2017a). In addition, AA can affect the surface
60 and atmospheric temperature by altering the radiative properties of clouds through
61 aerosol-cloud interaction (Hansen et al. 1997; Stevens and Feingold 2009), and by
62 scattering and absorbing the solar radiation directly through aerosol-radiation

63 interaction. Additionally, remote AA emissions can impact on local temperature and
64 temperature extremes through changing dynamics. For example, the remote AA
65 emissions over Europe have a downstream extension impact on the temperature and
66 temperature extremes over East Asia (Dong et al. 2015, 2016). Besides anthropogenic
67 aerosol emissions, natural aerosol emissions can also influence climate dynamics (e.g.,
68 Yang et al., 2016, 2017).

69 The previous studies have highlighted external forcings, particularly anthropogenic
70 changes, play an important role in decadal changes of temperature extremes. However,
71 the relative individual contributions of changes in GHG concentrations and AA
72 emissions to the observed changes in temperature extremes are still not clear. Therefore,
73 the main aims of this work are to quantify the relative roles of changes in GHG and AA
74 forcing in shaping the changes in temperature extremes over China, and to understand
75 the physical processes responsible.

76 Despite the rapid development of attribution studies in climate extremes in recent
77 years (Stott et al. 2016), there is still no consensus about the best methodology for
78 attribution. One widely-used attribution approach relies on an atmospheric general
79 circulation model (AGCM) forced by prescribed sea surface temperatures (SSTs), with
80 and without anthropogenic influences (e.g., Christidis et al. 2013; Kamae et al. 2014;
81 Kim et al. 2015; Schaller et al. 2016). A potential limitation of these experiments is the
82 lack of explicit air–sea interaction, which causes an inconsistency in surface energy
83 fluxes and can limit a model's ability to accurately simulate natural climate variability

(e.g., Barsugli and Battisti 1998; He and Soden 2016). Another ordinary attribution method is bases on a coupled general circulation model (CGCM) with constant emissions, which reaches equilibrium after a long integration (Bollasina et al. 2011; Li and Ting 2016; Wang et al. 2012, 2013). The experiments in CGCMs with full ocean dynamics have huge computational cost. Moreover, the CGCMs may exhibit significant biases in the mean state, such as a large cold equatorial SST bias in Pacific (Vanniere et al. 2012). Thus, replacing the three-dimension ocean GCM with an ocean mixed-layer model would reduce the cost of the experiments, and have a smaller SST bias (due to a prescribed flux correction), whilst also retaining intra-seasonal variability and coupling between the atmosphere and the ocean. Therefore, this work is based on a set of experiments using an atmosphere-ocean-mixed-layer couple model (Hirons et al. 2015; Tian et al. 2018).

The structure of this paper is organized as follows: Section 2 illustrates the observed decadal changes in temperature extremes over China. The model and experiments are described briefly in Section 3. Section 4 evaluates the simulated changes in response to changes in GHG concentrations and AA emissions. Sections 5 and 6 illustrate the physical processes involved in the responses of hot and cold extremes to changes in anthropogenic forcings, respectively. Conclusions are summarized in Section 7.

2. Observed decadal changes in temperature extremes over China

2.1 Observational datasets

The China stations data used are the homogenized datasets of daily maximum temperature (Tmax) and minimum temperature (Tmin) series with 753 stations in China from 1960 to 2016 (Li et al. 2016). Considering various climate types in China, we divide the 753 stations into three sub-regions: Northern China (NC) with 331 stations north of 35ºN, Southeastern China (SEC) with 334 stations south of 35ºN and east of 105ºE, and Southwestern China (SWC) with 88 stations south of 35ºN and west of 105ºE. The distributions of these three sub-regions are shown in Fig. 2a. Also used are the global land gridded climate extremes (GHCNDEX) based on the Global Historical Climatology Network (GHCN)-Daily dataset from 1960 to 2011 (Donat et al. 2013). The hot extremes indices are annual hottest day temperature (TXx), and warmest night temperature (TNx), the frequency of summer days (SU, annual number of days when Tmax >25ºC), and tropical night (TR, annual number of days when Tmin >20 ºC). The cold extremes indices are annual coldest day temperature (TXn), and coldest night temperature (TNn), the frequency of ice days (ID, annual number of days when Tmax <0 ºC), and frost days (FD, annual number of days when Tmin <0 ºC).

2.2 Observed decadal changes since the mid-1990s

Figure 1 illustrates the time evolution of the area averaged annual mean temperature extremes anomalies over China and over three sub-regions, relative to the

123 climatology, averaged over the whole time period. These time series clearly show the
124 abrupt changes in both hot and cold extremes since the mid-1990s. Therefore, the
125 decadal change in this study is compared between present day (PD) of 1994~2011 and
126 early period (EP) of 1964~1981. During summer, a rapid increase in TXx since the mid-
127 1990s occurs in China (Fig. 1a). The change in TXx anomaly during the PD relative to
128 the EP is 0.57 ºC in China station data, which is about two times as large as its
129 interannual variation of 0.27 ºC. This robust increase is also supported by the
130 GHCNDEX data with a change in TXx anomaly of 0.77 ºC. Additionally, the increase
131 of TXx from the EP to the PD occurs in each sub-region over China, with a range of
132 changes from 0.40 ºC to 0.76 ºC. Moreover, accompanied with the increase of TXx, the
133 frequency of SU rises by 9 days over China (8 days in GHCNDEX data; Fig. 1c).
134 Similar to the increase of TXx, TNx also shows significant increase over China since
135 the mid-1990s (Fig. 1b). The change in TNx anomaly is 0.76 ºC (0.96 ºC in GHCNDEX
136 data). The remarkable decadal increase of TNx occurs in individual sub-regions over
137 China, with the greatest amplitude of 1.05 ºC over NC and the smallest amplitude of
138 0.52 ºC over SEC. The frequency of TR rises by 8 days in China (Fig. 1d), coinciding
139 with the increase of TNx.

140 During winter, the cold extremes also exhibit decadal changes since the mid-1990s,
141 being characterized as a rise in temperature and a decrease in frequency of cold days.
142 TXn anomaly increases by 1.48 ºC over China (Fig. 1e), being similar to the change of
143 1.45 ºC in GHCNDEX data. The increase of TXn manifests over three sub-regions with

144 a range from 0.94 ºC to 1.59 ºC. As a result of the increase of TXn, the frequency of ID
145 is decreased by about 4 days over China (Fig. 1g). The decrease in ID is mainly over
146 NC, with the magnitude of 8 days. Moreover, a robust increase in TNn appears since
147 the mid-1990s. The changes of TNn anomaly is 1.82 ºC over China, being consistent
148 with 1.86 ºC in GHCNDEX data (Fig. 1f). The greatest increase of TNn is over NC
149 (2.17 ºC). Additionally, the frequency of FD is decreased by about 10 days (Fig. 1h). It
150 is noted that the changes in cold extremes are larger than hot extremes. This is consistent
151 with stronger seasonal warming over northern hemisphere mid-latitudes in boreal
152 winter than in boreal summer in response to anthropogenic forcing (e. g., John et al.
153 2012; Dong et al. 2017b), which is related to the snow-albedo feedback (e.g., Stouffer
154 and Wetherald 2007; Rangwala et al. 2016).

155 The spatial patterns of changes in these temperature extremes during the PD
156 relative to the EP are illustrated in Fig. 2. The most important features of changes are
157 the increase in hot extremes and decrease in cold extremes over the most regions of
158 China although there are some spatial variations (Figs. 2b-i). For the hot extremes, the
159 changes in TXx and TNx show a large increase over NC with a magnitude of about
160 1.0~1.5 ºC (Figs. 2b and c). While the changes in the frequencies of SU and TR show
161 the increase in a large domain over SEC (Figs. 2d and e). For the cold extremes, the
162 TXn and TNn show a relatively uniform increase over China with a range of 1.5~2.5
163 ºC (Figs. 2f and g). The frequencies of ID and FD show a decrease over the most regions
164 of China (Figs. 2h and i).

The robust decadal changes in the temperature extremes have been observed over China since the mid-1990s. Questions come out naturally: what has caused these rapid changes? Do the anthropogenic activities drive these changes? A set of experiments using a coupled climate model are performed to assess contributions of changes in anthropogenic forcings (GHG concentrations and AA emissions) to observed decadal changes in temperature extremes over China since the mid-1990s, and to quantify the relatively roles of individual forcing factors and to elucidate physical processes involved.

3. Model and experiments design

The model used is an atmosphere-ocean-mixed-layer coupled model called MetUM-GOML1 (Hirons et al. 2015). The atmospheric component is the Met Office Unified Model (MetUM) at the fixed scientific configuration Global Atmosphere 3.0 (GA3.0; Arribas et al. 2011; Walters et al. 2011) with a horizontal resolution of 1.875° longitude and 1.25° latitude.

The model includes earth system components such as an interactive tropospheric aerosol scheme and the following aerosol: ammonium sulphate, mineral dust, sea salt, fossil fuel black carbon, fossil fuel organic carbon, biomass burning aerosols, and secondary organic (biogenic) aerosols. The direct radiative effect due to scattering and absorption of radiation by all aerosol species is represented in the model. The semi-direct effect, whereby aerosol absorption tends to change cloud formation by warming the aerosol layer, is included implicitly (Walters et al. 2011). The parameterization of

186 the indirect effects is described in detail by Jones et al. (2011). The model validation
187 suggested a good performance in simulating aerosol properties and the detailed
188 description of this aspect has been documented in Bellouin et al. (2011). The modeled
189 sulphate aerosol surface concentrations, nitrate aerosol concentrations, carbonaceous
190 aerosol concentrations and total AODs are all compares well against observed
191 measurements. Moreover, the model reproduced the known pattern of AOD, with
192 industrial pollution in North America, Europe, and Asia, biomass burning aerosols in
193 Central Africa and South America, and mineral dust transport across the Atlantic and
194 Arabian Sea. The eastward gradient in AOD in North America and China is well
195 reproduced.

196 The oceanic component is a Multi-Column K Profile Parameterization (MC-KPP)
197 mixed-layer ocean model. The atmospheric and oceanic components are coupled every
198 three hours. The air–sea coupling is limited by the maximum extent of a seasonally
199 varying sea ice climatology (Hirons et al. 2015). In the uncoupled region of MetUM-
200 GOML1, the atmosphere is forced by the repeating mean annual cycle of SST and sea
201 ice extent (SIE) from the Met Office HadISST data set (Rayner et al. 2003). The
202 horizontal resolution of MC-KPP is the same as the MetUM where it is coupled. The
203 MC-KPP columns have 100 vertical levels with a depth of 1000m. The vertical
204 discretization allows very high resolution (approximately one meter) in the upper ocean.
205 Since MC-KPP simulates only vertical mixing and does not include ocean dynamics,
206 climatological seasonal cycles of depth-varying temperature and salinity corrections are

207 prescribed to represent the mean ocean advection and account for biases in atmospheric
208 surface fluxes.

209 Since the mid-1990s, there have been increased anthropogenic GHG
210 concentrations (14% increase in CO_2, 23% increase in CH_4 and 7% increase in N_2O),
211 and significant changes in AA emissions. The changes in annual mean sulfur dioxide
212 emissions are characterized as decreases over Europe and North America and increases
213 over East and South Asia (Fig. 3).

214 As summarized in Table 1, a 12 year MetUM-GOML1 relaxation experiment (R0)
215 was firstly performed in which the MC-KPP profiles of temperature and salinity were
216 relaxed to a present day (PD; 1994~2011) ocean temperature and salinity climatology
217 derived from the Met Office ocean analysis (Smith and Murphy 2007). The relaxation
218 experiment used PD GHG and AA forcings (Lamarque et al. 2010, 2011). The daily
219 mean seasonal cycle of ocean temperature and salinity corrections from the coupled
220 relaxation experiment are then imposed in free-running coupled experiments. Four
221 other experiments are performed by using different forcings. These experiments
222 represent the early period (EP; 1964~1981), All Forcing present day (PDGA), GHG
223 forcing (PDG) and AA forcing (PDA) with no relaxation. All experiments are run for
224 50 years and use the climatological PD sea ice extent from HadISST (Rayner et al.
225 2003). The last 45 years of each experiment are used for analysis. Using the same set
226 of experiments, Tian et al. (2018) has investigated the responses of the East Asian
227 summer monsoon.

The response to a particular forcing is estimated by the difference between a pair of experiments that include and exclude that forcing. The combined effect of changes in both GHG and AA (hereafter All forcing) is the difference between PDGA and EP experiment (PDGA - EP). The impact of changes in GHG concentrations (hereafter GHG forcing) is the difference between PDG and EP (PDG - EP) and the impact of changes in AA emissions (hereafter AA forcing) is the difference between PDA and EP (PDA - EP).

4. Model simulated changes in response to anthropogenic forcing

The spatial distributions of changes in hot extremes in response to different forcings are shown in Fig. 4. The model experiment in response to changes in All forcing from the EP to the PD, not only reproduces the significant increase of hot extremes over China, but also captures the generally spatial patterns of observed changes (Figs. 4a-d). The increase of TXx and TNx in response to All forcing changes exceeds 0.5 ºC over the most area of China (Figs. 4a and b), with a maximum center over NC (exceed 1.0 ºC), being consistent with observations (Figs. 2b and c). As a result, the frequencies of SU and TR manifest a significant increase over China in response to All forcing changes (Figs. 4c and d). The large increase domain is over SEC, which is also seen in observations (Figs. 2d and e). The similarities between the changes in response to All forcing and observed changes indicate that the observed increase in hot extremes over China since the mid-1990s is predominantly due to the anthropogenic

248 GHG and AA changes.

249 Moreover, in response to the GHG forcing change, the hot extremes show a more
250 or less uniform increase over China (Figs. 4e-h). The spatial pattern and magnitude of
251 changes in hot extremes in response to GHG forcing changes are similar to those in
252 response to All forcing changes, indicating that changes in GHG concentrations play a
253 dominant role in the increase in hot extremes over China. Nevertheless, the role of
254 changes in AA forcing in the hot extremes is relatively weak and shows a dipole pattern
255 with increases in north and decreases in south (Figs. 4i-l). The increase in TXx and TNx,
256 as well as the increase in the frequencies of SU and TR, is shown over NC in response
257 to changes in AA forcing, although the magnitude is weaker than that in response to
258 changes in GHG forcing. However, the decrease in TXx, TNx and frequencies of SU
259 and TR appears over SEC and SWC in response to changes in AA forcing.

260 In terms of the cold extremes, their responses to changes in different forcings are
261 illustrated in Fig. 5. The rise in TXn and TNn and the decrease in the frequencies of ID
262 and FD in response to All forcing changes coincide with observations (Figs. 5a-d). In
263 response to changes in GHG forcing, the increase in TXn and TNn and the decrease in
264 the frequencies of ID and FD are not only comparable to those in response to All forcing
265 changes, but also consistent with those in observations (Figs. 5e-h), suggesting that
266 GHG forcing changes play a vital role in the observed decadal changes of cold extremes.
267 Additionally, AA forcing changes also contribute to changes in cold extreme (Figs. 5i-
268 l), particularly to the rise in TXn and TNn and decrease in frequencies of ID and FD

over NC and SEC, although the magnitudes of changes are weaker than those in response to GHG forcing changes.

Quantitatively, the model simulated changes in response to All forcing changes reproduce the observed changes in temperature extremes over China realistically, although some extreme indices are overestimated a little bit. In response to All forcing changes, the area averaged TXx (TNx) over China is 1.05 ºC (0.92 ºC), which are comparable to the observed changes of 0.58 ºC (0.76 ºC). The TXn and TNn averaged over China in response to All forcing changes are 1.69 ºC and 1.45 ºC, which are very close to observed changes of 1.48 ºC and 1.82 ºC.

Moreover, the agreement of model simulated magnitude of changes in extreme indices with those in observations is not only over China as a whole, but also over individual sub-regions. Figure 6 gives some area averaged changes in temperature extreme indices over the three sub-regions for both observations and model simulated responses. The area averaged changes in TXx in response to All forcing changes are comparable to observations, although they are overestimated a little bit over NC and SEC. The simulated TNx changes are also in good agreement with the observations, particularly over NC. The change of TNx over NC in response to All forcing changes is 1.07 ºC, compared to the observed change of 1.05 ºC. Additionally, the increases in frequencies of SU and TR in response to All forcing changes are very similar to those in observations in each sub-region. On the other side, the model simulated changes of cold extremes in response to All forcing changes over the three sub-regions are in good

290 agreement with observations. The TXn (TNn) is 2.26 ºC (1.84 ºC) over NC, 1.28 ºC
291 (1.07 ºC) over SEC and 0.64 ºC (0.82 ºC) over SWC, which are very close to observed
292 changes of 1.59 ºC (2.17 ºC) over NC, 1.52 ºC (1.59 ºC) over SEC and 0.94 ºC (1.36
293 ºC) over SWC. The decrease of frequencies of ID and FD also coincides with
294 observations.

295 Separately, the model simulated response to GHG forcing changes exhibit increase
296 in hot extremes over all the three sub-regions. The magnitude of this increase in
297 response to GHG forcing changes is almost equal to that in response to All forcing
298 changes, indicating a dominant contribution of changes in GHG concentrations to the
299 simulated increase in hot extremes over China. On the contrary, the simulated responses
300 of hot extremes in response to AA forcing changes show positive value over NC but
301 negative value over SEC, which are consistent with the dipole pattern with increases in
302 north and decreases in south (Figs. 4i-l). In terms of cold extremes, the model simulated
303 increase in cold temperatures and decrease in frequencies of cold days result from the
304 combined effects of changes in both GHG concentrations and AA forcing . The
305 simulated change of TXn and TNn in response to GHG forcing changes is about two to
306 three times that in response to AA forcing changes. The simulated changes in TXn
307 (TNn) are 2.03 ºC (1.08 ºC) over NC and 1.21 ºC (1.71 ºC) over SEC in response to
308 GHG forcing changes, in comparison to 0.76 ºC (0.55 ºC) over NC and 0.64 ºC (0.5 ºC)
309 over SEC in response to AA forcing changes.

310 There is a nonlinearity for some extreme temperature changes in response to

311 changes in GHG concentrations and AA forcing in model simulations, i.e., the sum of
312 responses to separate forcings is not equal to the response to changes in All forcings
313 together. This nonlinearity is weak over NC. The increase of extremes over NC in
314 response to changes in GHG forcing explains up to 75% of the TNx, 90% of the TXn
315 and 60% of the TNn increase in response to All forcing (assuming linearity). But the
316 nonlinearly is clearly shown for some temperature extremes over SEC (Fig. 6c), and ID
317 and FD over SWC (Fig. 6f). The nonlinearity of responses to different forcings has
318 noticed by previous studies (Feichter et al. 2004; Ming and Ramaswamy 2009;
319 Shiogama et al. 2012). They suggested that the nonlinear cloud response is likely the
320 source for this nonlinearity. The response of cloud water content and cloud radiative
321 effect have strong dependency in the combined forcing experiment than in either of the
322 individual forcing experiments. In our study, the large nonlinearity is over SEC, where
323 the water vapor content is high. The high humidity tends to increase the nonlinear cloud
324 response to the anthropogenic forcing. However, detailed discussion of this nonlinearity
325 is beyond the scope of this study.

326 The simulated response to changes in All forcing indicates that anthropogenic
327 changes play an important role in generating observed decadal changes in temperature
328 extremes. However, the responses to changes in GHG and AA show some different
329 characteristics. Model results indicate that GHG forcing changes tend to increase both
330 hot and cold extreme temperatures TXx, TNx, TXn, and TNn, increase frequency in
331 SU and TR, and decrease in ID and FD over China, while AA forcing changes are likely

to warm NC and cool SEC during summer and induce surface warming over NC and SEC during winter. The physical processes responsible for the changes in hot and cold extremes in response to different forcings are discussed in next sections, respectively.

5. Physical processes responsible for the decadal changes of hot extremes

5.1 Induces by GHG forcing changes

The spatial patterns of summer mean changes for the key components of surface energy balance and related variables induced by changes in GHG forcing are illustrated in Fig. 7. The direct impact of the increase in GHG concentrations leads to an increase of clear sky downward longwave (LW) radiation of 0.94 W m^{-2} over China (Fig. 7a; as expected for an increase in the Greenhouse Effect), although part of this increase would be compensated by increase of upward surface LW radiation (-0.49 W m^{-2}) since surface warming (Fig. 7b). The net LW anomaly tends to reflect a balance between the increase emission from the warmer surface (Fig. 7a) and the negative LW cloud radiative effect (LW CRE; not shown), as a consequence of reduction in cloud cover (Figs. 7c and d). The decrease in cloud cover over land is related to the decrease in relative humidity (not shown) since specific humidity over land increases less (reduction of evapotranspiration related to the CO_2 physiological effect and constrained by ocean warming) than specific humidity at saturation which increases with the continental surface temperature following the Clausius-Clapeyron relationship (e.g., Dong et al. 2009; Boé and Terray 2014). The reduction of cloud cover and decrease of

relative humidity, being likely due to the surface warming, lead to positive shortwave cloud radiative effect (SW CRE; with the value of 1.62 W m^{-2}; Fig. 7e) and positive net surface shortwave (SW) radiation (with the value of 0.95 W m^{-2}; Fig. 7f) over the most part of China, which in turn have a positive feedback on surface warming. In summary, it is the increased Greenhouse Effect that induces the increase in hot extremes over China, with increase of the net downward clear sky LW radiation, in response to GHG forcing changes. Moreover, the increase of net surface SW radiation related to positive SW CRE, being associated with the decrease of cloud cover, has a positive feedback with the surface warming due to the increase of GHG concentrations, which also contributes to the increase of hot extremes over China.

5.2 Induced by AA forcing changes

The spatial distributions of the summer mean changes for the key components of surface energy balance and related variables induced by changes in AA emissions are illustrated in Fig. 8. Changes in aerosol optical depth (AOD) indicate a decrease over Europe and an increase over East Asia and South Asia (Fig. 8a). Local increase of AOD over East Asia leads to decrease of net clear sky SW radiation (-3.36 W m^{-2}) over China through aerosol-radiation interactions (Fig. 8b). However, the SW CRE changes show positive anomaly, particularly over NC with a magnitude of 1.22 W m^{-2} (Fig. 8c). This positive SW CRE warms the surface and leads to increase in hot extremes over NC while the decrease of net surface SW radiation through AA induced net clear sky SW radiation change cools the surface and leads to decrease in hot extremes over SEC. The

positive SW CRE over NC is induced by the decrease of cloud cover (Fig. 8d), which is related to the decrease of soil moisture (Fig. 8d) and water vapor in the atmosphere (Fig. 8f). This is consistent with Tian et al. (2018), who suggested a drying over NC related to a weakening of East Asian summer monsoon (EASM) in response to AA forcing changes. The weakening of EASM is associated with weaker moisture transport convergence and reduced precipitation (not shown), soil moisture (Fig. 8e) and evaporation (not shown) over NC, leading to decrease in water vapor in the atmosphere (Fig. 8f), which in turn gives rise to the positive SW CRE, as a consequence of decrease in cloud cover. In summary, direct impact of changes in AA forcing induces a decrease in clear sky SW radiation, which results in surface cooling over SEC and SWC. However, the positive SW CRE and reduced upward latent heat flux (not shown), induced by decrease of cloud cover related to reduction of precipitation over NC and decrease of soil moisture, tend to warm the surface and contribute to increase in hot extremes over NC.

6. Physical processes responsible for the decadal changes of cold extremes

6.1 Induces by GHG forcing changes

Figure 9 is the spatial distributions of the winter mean changes for the key components of surface energy balance and related variables induced by changes in GHG concentrations. The downward clear sky LW radiation is increased over southern part of China with the value of 0.66 W m^{-2} (Fig. 9a), although part of this increase is

likely to be compensated by the increase of upward surface LW radiation due to surface warming (Fig. 9b). The positive change of net clear sky LW radiation is partly due to direct impact of incease in GHG concentrations and partly due to increases of water vapor in the atmosphere related to GHG induced ocean warming (Fig. 9c). Furthermore, the net surface SW radiation is increased over northern part of China (Fig. 9d), which is mainly due to the increase of net clear sky SW radiation (Fig. 9e). The positive clear sky SW radation, with a vaule of 4.5 W m^{-2} over NC, results from snow albedo feedback through the reduction of snow cover and depth due to skin temperature warming (Fig. 9f; e.g., Robock 1983; Yang et al. 2001; Bony et al. 2006; Qu and Hall 2007; Thackeray and Fletcher 2016). In summary, the positive change in net clear sky LW radiation due to the Greenhouse Effect and associated water vapor feedback contribute to the warming over SWC and SEC and leads to changes in cold extremes. The increase of net surface SW radiation, mainly due to the increase of clear sky SW radiation related to decrease in snow cover and depth, leads to large changes in day-time extremes of TXn and ID than night-time extremes of TNn and FD over NC.

6.2 Induced by AA forcing changes

Figure 10 is the spatial distributions of the winter mean changes for the key components of surface energy balance and related variables induced by changes in AA emissions. During winter, AA are advected by mean flow to the Indian Ocean and western North Pacific, instead of that the AA effects are more over emission area due to relatively weak advections during summer. There is significant cooling over the

414 Indian Ocean and western North Pacific (Fig. 10a) results from the increased AA
415 advected by prevailing winds from South and East Asia. This cooling corresponds to
416 the decrease of water vapor extending from western North Pacific to East Asia (Fig.
417 10b). The decrease of water vapor in the atmosphere results in decrease of cloud cover
418 over Eastern China (Fig. 10c), which induces positive SW CRE (Fig. 10d). The
419 positive SW CRE, with a magnitude of 4.01 W m^{-2} over NC and SEC, contributes to
420 the local surface warming (Fig. 10a) and decrease in cold extremes over NC and SEC.
421 In addition, the decrease of upward latent heat flux (Fig. 10e; 1.33 W m^{-2}), as a
422 consequences of decrease in evaporation (Fig. 10f), also makes a contribution to the
423 surface warming and a contribution to increase in TXn and TNn and decrease in
424 frequencies of ID and FD over SEC.

425 **7. Conclusions**

426 We found significant decadal changes in both hot and cold extremes over China
427 since the mid-1990s by using Chinese observed station dataset. These changes are
428 characterized as the rise in TXx, TNx and the increase in frequencies of SU and TR
429 during summer, and the rise in TXn and TNn and the decrease in frequencies of ID and
430 FD during winter. In this study, we have performed a set of experiments using an
431 atmosphere-ocean-mixed-layer coupled model to assess the contributions of All forcing
432 changes, as an combined effects of GHG and AA forcing, to observed decadal changes
433 in temperature extremes over China across the mid-1990s, and quantify the relatively
434 roles of changes in GHG concentrations and AA emissions, respectively. The main

435 conclusions are as follow.

436 Observations indicate that there was an abrupt change in temperature extremes over
437 China since the mid-1990s. The changes of temperature extremes are analyzed by the
438 comparison between the PD of 1994~2011 and the EP of 1964~1981. Spatially
439 averaged over China, the hot extremes of TXx and TNx are increased by 0.58 ºC and
440 0.76 ºC, respectively. The frequencies of SU and TR are increased by about 7~9 days.
441 The cold extremes of TXn and TNn are increased by 1.48 ºC and 1.82 ºC, respectively.
442 The frequencies of ID and FD are decreased by about one week. Furthermore, these
443 abrupt decadal changes occur not only over China as a whole, but also over three sub-
444 regions of NC, SEC and SWC, even though they exhibit various climate types.

445 The atmosphere-ocean-mixed-layer coupled model MetUM-GOML1 in response
446 to changes in GHG concentrations and AA emissions together (All forcing) realistically
447 reproduces the spatial patterns of the observed decadal changes in both hot and cold
448 temperature extremes. Quantitatively, the model simulated changes in response to All
449 forcing changes are comparable to the observed decadal changes. The results indicate
450 a dominant role of anthropogenic changes in the observed decadal changes of
451 temperature extremes over China across the mid-1990s.

452 Moreover, model responses to changes in GHG concentration and AA emissions
453 show some different characteristics. GHG forcing changes lead to increase in hot
454 extremes (TXx, TNx, SU and TR), and TNx and TNn and decrease in frequencies of
455 ID and FD over China, while AA forcing changes lead to weak increases in hot extremes

over NC and decrease over SEC during summer and induce changes in cold extremes the same sign as those induced by GHG over NC and SEC during winter, but with weak magnitude. The responses of cold extremes in response to changes in GHG forcing are two to three times as large as those in response to changes in AA forcing, indicating a dominant role of GHG forcing changes in the model simulated cold extreme changes in response to All forcing changes. Relatively, the increase of extremes over NC in responses to changes in GHG forcing explains up to 75% of the TNx, 90% of the TXn and 60% of the TNn increase in response to changes in All forcing (assuming linearity). These results indicate that the model simulated extreme temperature changes in response to All forcing changes are predominantly induced by GHG forcing change, but AA change also makes some weak contributions.

In response to the increase of GHG concentrations, the increase of hot extremes is mainly due to the increased Greenhouse Effect with positive net surface clear sky LW radiation. Additionally, the increase of net surface SW radiation, mainly resulted from the positive SW CRE, associated with the decrease of cloud cover, has a positive feedback with the surface warming and the increase in hot extremes. In terms of changes in cold extremes in response to GHG forcing changes, the increase of net surface clear sky LW radiation due to the increased greenhouse effect and associated water vapor feedback tend to result in surface warming over southern part of China, and therefore lead to increase in TXn and TNn and decrease in frequencies of ID and FD. The changes of cold day-time extremes (TXn and ID) over NC are further enhanced

by the increase of clear sky SW radiation related to the decrease of snow-albedo feedback.

During summer, the response of hot extremes over China to changes in AA forcing exhibits a dipole pattern with increases in north and decreases in south. Local increase of AOD over East Asia leads to decrease of net clear sky SW radiation, which tends to cool the surface. However, the positive SW CRE tends to warm the surface and leads to increase in hot extremes over NC. The positive SW CRE is induced by the decrease of cloud cover, which related to the decrease of soil moisture, as a consequence of reduction in precipitation over NC, while decreases in hot extremes over South China are the results of direct impacts of AA forcing changes through aerosol-radiation and aerosol-cloud interactions due to increased AA emissions over East Asia. During winter, AA are advected by mean flow to the Indian Ocean and western North Pacific, which induces cooling over there. This cooling reduces water vapor and therefore reduces cloud cover over East Asia, leading to positive SW CRE over NC and SEC and therefore leading to increase in TXn and TNn and decrease in frequencies of ID and FD over NC and SEC.

In this study, besides the cooling effect by the direct impacts of AA forcing changes through aerosol-radiation and aerosol-cloud interactions, we find a surface warming over NC during summer and over China during winter driven by AA forcing changes through the AA induced atmosphere-cloud feedback. This aerosol-climate interaction is consistent with Tian et al. (2018)..

Our results suggested the different roles of GHG and AA in temperature extremes. The model shows a strong warming over China in response to GHG forcing, and a cooling over SC and a weak warming over NC in response to AA forcing during summer. In addition, previous studies have pointed out different roles of GHG and AA in shaping the temperature trend over China by using CMIP5 models. The CMIP5 experiments result suggested that the GHG plays a dominant role in the warming trend over China (e.g., Song et al. 2014; Zhao et al. 2015), which is consistent with our model result. Zhao et al. (2015) showed that the AA forcing has a cooling effect, and they further indicated that the individual effects of AA cannot be detected in the observed temperature changes with respect to the combined effects among all the other forcings, implying an uncertainty about the AA forcing impact in their study. In addition, Li et al. (2015) further suggested that the indirect AA effect (including indirect, semidirect, surface albedo effects, and so on) induce warming over NC, which also can seen by our model result.

The results in this study indicate a remarkable role of anthropogenic changes, especially the increased GHG concentrations, in the observed decadal changes of temperature extremes over China since the mid-1990s. Given the fact that GHG concentrations and local AA emissions will continue to rise in the next few decades, observed recent decadal changes in temperature extremes over China are likely to sustain, or even amplify in the near future.

519 **Acknowledgement**

520 This study is supported by the National Natural Science Foundation of China under
521 Grants 41675078, U1502233, 41320104007, by the Youth Innovation Promotion
522 Association of CAS (No. 2018102) and by the UK-China Research & Innovation
523 Partnership Fund through the Met Office Climate Science for Service Partnership
524 (CSSP) China as part of the Newton Fund. BD is supported by the U.K. National Centre
525 for Atmospheric Science–Climate (NCAS-Climate) at the University of Reading. The
526 authors thank Editor Jian Lu and anonymous reviewers for their constructive comments
527 on the earlier version of the paper.

528 **Reference**

529 Alexander LV et al (2006) Global observed changes in daily climate extremes of
530 temperature and precipitation. J Geophys Res 111**:**D05109. doi:
531 10.1029/2005JD006290

532 Arribas A et al (2011) The GloSea4 ensemble prediction system for seasonal forecasting.
533 Monthly Weather Review 139(6):1891–1910

534 Barsugli J, Battisti D S (1998) The basic effects of atmosphere–ocean thermal coupling
535 on midlatitude variability. J Atmos Sci 55:477–493. doi:10.1175/1520-0469

536 Bellouin N, Rae J, Jones A, Johnson C, Haywood J, Boucher O (2011) Aerosol forcing
537 in the climate model intercomparison project (CMIP5) simulations by
538 HadGEM2-ES and the role of ammonium nitrate. J Geophys Res 116:D20206.
539 doi: 10.1029/2011JD016074

540 Boé J, Terray L (2014) Land–sea contrast, soil-atmosphere and cloud-temperature
541 interactions: interplays and roles in future summer European climate change.
542 Clim Dyn 42:683–699

543 Bollasina MA, Ming Y, Ramaswamy V (2011) Anthropogenic aerosols and the
544 weakening of the South Asian summer monsoon. Science 334(6055):502–505

545 Bony S et al (2006) How well do we understand and evaluate climate change feedback
546 processes? J Clim 19(15):3445–3482. doi: 10.1175/jcli3819.1

547 Christidis N et al (2013) A new HadGEM3-A-based system for attribution of weather
548 and climate-related extreme events. J Clim 26:2756–2783. doi:10.1175/JCLI-D-

549 12-00169.1
550 Cubasch U et al (2001) Projections of future climate change. Climate Change 2001:
551 The Scientific Basis, J. T. Houghton et al., Eds., Cambridge University Press
552 525–582
553 Donat MG, Alexander LV, Yang H, Durre I, Vose R, Caesar J (2013) Global land-based
554 datasets for monitoring climatic extremes. Bull Am Meteorol Soc 94:997–1006.
555 doi:10.1175/BAMS-D-12-00109.1
556 Dong BW, Sutton RT, Shaffrey L (2017a) Understanding the rapid summer warming
557 and changes in temperature extremes since the mid-1990s over Western Europe.
558 Clim Dyn 48:1537–1554. doi:10.1007/s00382-016-3158-8
559 Dong BW, Sutton RT, Shaffrey L, Klingaman NP (2017b) Attribution of forced decadal
560 climate change in coupled and uncoupled ocean-atmosphere model experiments.
561 J Clim doi:10.1175/JCLI-D-16-0578.1
562 Dong BW, Sutton RT, Chen W, Liu XD, Lu RY, Sun Y (2016) Abrupt summer warming
563 and changes in temperature extremes over Northeast Asia since the mid-1990s:
564 Drivers and physical processes. Adv Atmos Sci 33(9):1005–1023. doi:
565 10.1007/s00376-016-5247-3
566 Dong BW, Sutton RT, Highwood E, Wilcox L (2015) Preferred response of the East
567 Asian summer monsoon to local and nonlocal anthropogenic sulphur dioxide
568 emissions. Clim Dyn doi:10.1007/s00382-015-2671-5
569 Dong BW, Gregory JM, Sutton RT (2009) Understanding land-sea warming contrast in

response to increasing greenhouse gases. Part I: Transient adjustment. J Clim 22:3079-3097

Dwyer JG, Biasutti M, Sobel AH (2012) Projected changes in the seasonal cycle of surface temperature. J Clim 25(18):6359–6374

Feichter J, Roeckner E, Lohmann U, Liepert B (2004) Nonlinear aspects of the climate response to greenhouse gas and aerosol forcing. J Clim 17:2384–2398

Freychet S, Tett S, Wang J, Hegerl G (2017) Summer heat waves over eastern china: dynamical processes and trend attribution. Environ Res Lett 12:1–9. doi: 10.1088/1748-9326/aa5ba3

Hansen J, Sato M, Ruedy R (1997) Radiative forcing and climate response. J Geophys Res 102:6831–6864. doi:10.1029/96JD03436

He J, Soden B (2016) Does the lack of coupling in SST-forced atmosphere-only models limit their usefulness for climate change studies? J Clim 29:4317–4325. doi:10.1175/JCLI-D-14-00597.1

Hirons LC, Klingaman NP, Woolnough SJ (2015) MetUM-GOML: a near-globally coupled atmosphere–ocean-mixed-layer model. Geoscientific Model Development 8:363–379

Jones C et al (2011) The HadGEM2-ES implementation of CMIP5 centennial simulations. Geophys Model Dev 4:543–570

Kamae Y, Shiogama H, Watanabe M, Kimoto M (2014) Attributing the increase in

591 Northern Hemisphere hot summers since the late 20th century. Geophys Res Lett
592 41:5192–5199. doi:10.1002/2014GL061062
593 Kim YH, Min SK, Zhang X, Zwiers F, Alexander LV, Donat MG, Tung YS (2015)
594 Attribution of extreme temperature changes during 1951–2010. Clim Dyn
595 46:1769–1782. doi:10.1007/ s00382-015-2674-2
596 Lamarque JF et al (2010) Historical (1850–2000) gridded anthropogenic and biomass
597 burning emissions of reactive gases and aerosols: Methodology and application.
598 Atmos Chem Phys 10:7017–7039. doi:10.5194/acp-10-7017-2010
599 Lamarque JF et al (2011) Global and regional evolution of short-lived radiatively-active
600 gases and aerosols in the Representative Concentration Pathways. Climatic
601 Change 109:191–212. doi:10.1007/s10584-011-0155-0
602 Li CX, Zhao TB, Ying KR (2015) Effects of anthropogenic aerosols on temperature
603 changes in China during the twentieth century based on CMIP5 models. Theor
604 Appl Climatol doi: 10.1007/s00704-015-1527-6
605 Li X, Ting M (2016) Understanding the Asian summer monsoon response to
606 greenhouse warming: the relative roles of direct radiative forcing and sea surface
607 temperature change. Clim Dyn 49:1–18
608 Li Z et al (2016) Comparison of two homogenized datasets of daily
609 maximum/mean/minimum temperature in China during 1960–2013. J Meteor
610 Res 30(1):053–066. doi: 10.1007/s13351-016-5054-x
611 Ma SM, Zhou TJ, Stone D, Angelil O, Shiogama H (2017) Attribution of the July-

August 2013 heat event in central and eastern China to anthropogenic Greenhouse gas emissions. Environ Res Lett 12:054020

Ming Y, Ramaswamy V (2009) Nonlinear climate and hydrological responses to aerosol effects. J Clim 22:1329–1339

Otto FE, Massey, van Oldenborgh GJ, Jones RQ, Allen MR (2012) Reconciling two approaches to attribution of the 2010 Russian heat wave. Geophys Res Lett 39:L04702. doi:10.1029/2011GL050422

Perkins SE (2015) A review on the scientific understanding of heatwaves--their measurement, driving mechanisms, and changes at the global scale. Atmos Res 164:242–267

Qu X, Hall A (2007) What controls the strength of snow-albedo feedback? J Clim 20(15):3971–3981, doi: doi:10.1175/JCLI4186.1

Randall DA et al (1994) Analysis of snow feedbacks in 14 general circulation models. J Geophys Res Atmos 99(D10):20757–20771. doi: 10.1029/94jd01633

Rangwala I, Sinsky E, Miller JR (2016) Variability in projected elevation dependent warming in boreal midlatitude winter in CMIP5 climate models and its potential drivers**.** Clim Dyn 46:2115

Rayner NA et al (2003) Global analyses of sea surface temperature, sea ice, and night marine air temperature since the late nineteenth century. J Geophys Res 108:4407. doi:10.1029/2002JD002670

Robock A (1983) Ice and snow feedbacks and the latitudinal and seasonal distribution

633 of climate sensitivity. J Atmos Sci 40 (4):986–997
634 Schaller N et al (2016) Human influence on climate in the 2014 southern England
635 winter floods and their impacts. Nat Clim Change 6:627–634.
636 doi:10.1038/nclimate2927
637 Shiogama H, Stone DA, Nagashima T, Nozawa T, Emori S (2012) On the linear
638 additivity of climate forcing-response relationships at global and
639 continental scales. Int J Climatol 33:2542–50
640 Smith DM, Murphy JM (2007) An objective ocean temperature and salinity analysis
641 using covariances from a global climate model. J Geophys Res 112:C02022.
642 doi:10.1029/2005JC003172
643 Song F, Zhou T, Qian Y (2014) Responses of East Asian summer monsoon to natural
644 and anthropogenic forcings in the 17 latest CMIP5 models. Geophys Res Lett 41.
645 doi:10.1002/2013GL058705
646 Stevens B, Feingold G (2009) Untangling aerosol effects on clouds and precipitation in
647 a buffered system. Nat 461:607–613. doi:10.1038/nature08281
648 Stouffer RJ, Wetherald RT (2007) Changes of variability in response to increasing
649 greenhouse gases. part i: temperature. J Clim 20(21):5455
650 Stott et al (2016) Attribution of extreme weather and climate-related events. Wiley
651 Interdiscip. Rev Clim Change 7:23–41. doi:10.1002/wcc.380
652 Sun Y, Song LC, Yin H, Zhang XB. Stott P, Zhou BT, Hu T (2016) Human Influence
653 on the 2015 extreme high temperature events in western China [in “Explaining

654 Extreme Events of 2015 from a Climate Perspective"]. Bull Amer Meteor Soc
655 97:S5–S9.
656 Sun Y, Zhang X, Zwiers FW, Song L, Wan H, Hu T, Yin H, Ren G (2014) Rapid increase
657 in the risk of extreme summer heat in Eastern China. Nat Clim Change 4:1082–
658 1085. doi:10.1038/nclimate2410
659 Tian FX, Dong BW, Robson J Sutton RT (2018) Forced decadal changes in the East
660 Asian summer monsoon: the roles of greenhouse gases and anthropogenic
661 aerosols. Clim Dyn 6:1–17
662 Thackeray CW, Fletcher CG (2016) Snow albedo feedback: Current knowledge,
663 importance, outstanding issues and future directions. Prog Phys Geogr
664 40(3):392–408. doi: 10.1177/0309133315620999
665 Vannière BE, Guilyardi G, Madec FJ, Doblas R, Woolnough S (2013) Using seasonal
666 hindcasts to understand the origin of the equatorial cold tongue bias in CGCMs
667 and its impact on ENSO. Clim Dyn 40(3–4):963–981
668 Walters DN, Best MJ, Bushell AC, Copsey D, Edwards JM, Falloon PD, Roberts MJ
669 (2011) The met office unified model global atmosphere 3.0/3.1 and JULES
670 global land 3.0/3.1 configurations. Geosci Model Dev 4(4):919
671 Wang T et al (2013) Anthropogenic agent implicated as a prime driver of shift in
672 precipitation in eastern China in the late 1970s. Atmos Chem Phy 13(24):12433
673 Wang T, Otterå OH, Gao YG, Wang HJ (2012) The response of the North Pacific
674 Decadal Variability to strong tropical volcanic eruptions. Clim Dyn 39(12):2917–

675 2936

676 Wei K, Chen W (2011) An abrupt increase in the summer high temperature extreme
677 days across China in the mid-1990s. Adv Atmos Sci 28(5):1023–1029. doi:
678 10.1007/s00376-010-0080-6

679 Wen HQ, Zhang X, Xu Y, Wang B (2013) Detecting human influence on extreme
680 temperatures in China. Geophys Res Lett 40:1171–1176. doi:10.1002/grl.50285.

681 Wilcox LJ, Dong BW, Sutton RT, Highwood EJ (2015) The 2014 Hot, Dry Summer in
682 Northeast Asia [in "Explaining Extreme Events of 2014 from a Climate
683 Perspective"]. Bull Amer Meteor Soc 96(12):S105–S110. doi:10.1175/BAMS-
684 D-15-00123.1

685 Yang FL et al (2001) Snow-albedo feedback and seasonal climate variability over North
686 America. J Clim 14(22):4245–4248

687 Yang Y, Russell LM, Lou S, Lamjiri MA, Liu Y, Singh B, Ghan SJ (2016) Changes in
688 sea salt emissions enhance ENSO variability, J Clim 29:8575–8588.
689 doi:10.1175/JCLI-D-16-0237.1

690 Yang Y, Russell LM, Lou S, Liao H, Guo J, Liu Y, Singh B, Ghan SJ (2017) Dust-wind
691 interactions can intensify aerosol pollution over eastern China. Nat Commun
692 8:15333. doi:10.1038/ncomms15333

693 Yao Y, Luo Y, Huang JB (2012) Evaluation and projection of temperature extremes over
694 China based on CMIP5 model. Adv Clim Change Res 3(4). doi:
695 10.3724/SP.J.1248.2012.00179

696 Yin H, Sun Y, Wan H, Zhang XB, Lu CH (2016) Detection of anthropogenic influence
697 on the intensity of extreme temperatures in China. Int J Climatol 37:1229–1237.
698 doi: 10.1002/joc.4771
699 Zhao TB, Li CX, Zuo ZY (2016) Contributions of anthropogenic and external natural
700 forcings to climate changes over China based on CMIP5 model simulations. Sci
701 China Earth Sci 59:503–517. doi: 10.1007/s11430-015-5207-2
702 Zhou BT, Xu Y, Wu J, Dong S, Shi Y (2016) Changes in temperature and precipitation
703 extreme indices over China: analysis of a high-resolution grid dataset. Int J
704 Climatol 36:1051–1066

705 **Figure captions**

706 **Table 1.** Summary of numerical experiments.

707 **Figure 1.** Time series of annual mean temperature extremes anomalies relative to the
708 climatology (mean of the whole period) in summer (TXx, TNx, SU and TR; left
709 panels) and in winter (TXn, TNn, ID and FD; right panels) over China by GHCND
710 dataset (averaged over 20°~55°N, 75°~130°E; black solid lines) and by China
711 station dataset (averaged over 753 stations; red solid lines). The color dashed lines
712 represent the time series of temperature extremes anomalies averaged over three
713 sub-regions by China station dataset (see their distributions in Fig. 2a). Black
714 dashed range bars indicate the early period (EP) of 1964~1981 and the present day
715 (PD) of 1994~2011. Units in TXx, TNx, TXn, and TNn are °C. Units in SU, TR,
716 ID and FD are days.

717 **Figure 2.** (a) Distributions of 753 stations in China station dataset. The three sub-
718 regional groups are marked with different color dots. The dots in blue, purple and
719 green represent the sub-regions of Northern China (NC), Southeastern China (SEC)
720 and Southwestern China (SWC), respectively. (b)-(i) Spatial patterns of differences
721 in temperature extremes in summer (left panels) and in winter (right panels)
722 between the PD and the EP. The black lines indicate the regions where the changes
723 are statistically significant at the 90% confidence level base on *t*-test. Units in TXx,
724 TNx, TXn and TNn are °C. Units in SU, TR, ID and FD are days.

725 **Figure 3.** Differences in annual mean sulfur dioxide emissions (units: g m^{-2} yr^{-1})
726 between 1994~2010 and 1970~1981.

727 **Figure 4.** Spatial patterns of changes in hot extremes in response to changes in All
728 forcing (left panels), GHG forcing (middle panels) and AA forcing (right panels),
729 being masked by China boundary. The black lines indicate the regions where the
730 changes are statistically significant at the 90% confidence level base on *t*-test. Units
731 in TXx and TNx are °C. Units in SU and TR are days.

Figure 5. Same as Fig. 4, but for changes in cold extremes. Units in TNx and TNn are °C. Units in ID and FD are days.

Figure 6. Observed and model simulated changes in temperature extremes in response to different forcings over Northern China (a, b; NC, 35°~55°N, 75°~130°E), Southeastern China (c, d; SEC; 20°~35°N, 105°~130°E) and Southwestern China (e, f; SWC; 20°~35°N, 75°~105°E). The model simulated values have been masked by China boundary. The color bars indicate central estimates and dots show the 90% confidence intervals based on two-tailed Students'*t*-test. Top panels for TXx, TXn, TNx and TNn (units: °C) and bottom panels for SU, TR, ID and FD (units: days).

Figure 7. Spatial patterns of summer mean response to changes in GHG forcing: (a) clear sky LW radiation; (b) surface LW radiation; (c) total cloud cover (units: %) (d) low level cloud cover (units: %); (e) SW CRE; and (f) surface SW radiation. Radiation is the net component and in W m^{-2} with positive value meaning downward. The black lines highlight regions where the changes are statistically significant at the 90% confidence level base on *t*-test.

Figure 8. Spatial patterns of summer mean response to changes in AA forcing: (a) total AOD; (b) clear sky SW radiation; (c) SW CRE; (d) total cloud cover (units: %); (e) soil moisture (units: kg m^{-2}); and (f) column-integrated water vapor (units: kg m^{-2}). Radiation is the net component and in W m^{-2} with positive value meaning downward. The black lines highlight regions where the changes are statistically significant at the 90% confidence level base on *t*-test.

Figure 9. Spatial patterns of winter mean response to changes in GHG forcing: (a) clear sky LW radiation; (b) surface LW radiation; (c) column-integrated water vapor (units: kg m^{-2}); (d) surface SW radiation; (e) clear sky SW radiation; and (f) skin temperature (units: ºC). Radiation is the net component and in W m^{-2} with positive value meaning downward. The black lines highlight regions where the changes are statistically significant at the 90% confidence level base on *t*-test.

Figure 10. Spatial patterns of winter mean response to changes in AA forcing: (a) skin

760 temperature (units: ºC); (b) column-integrated water vapor (units: kg m^{-2}); (c) total
761 cloud cover (units: %); (d) SW CRE; (e) surface latent hear flux; and (f)
762 evaporation (units: kg m^{-2}). Radiation and flux are in W m^{-2} with positive value
763 meaning downward. The black lines highlight regions where the changes are
764 statistically significant at the 90% confidence level base on *t*-test.

Table 1. Summary of numerical experiments. Note that a slightly different period of 1970–1981 for the aerosol forcing in the early period is used since aerosol emissions data before 1970 were not available

Adv.	Experiment	Ocean	Radiative Forcing
R0	Relaxation run	Relaxation to "present day" (PD, 1994-2011) mean 3D ocean temperature and salinity to diagnose climatological temperature and salinity tendencies	PD greenhouse gases (GHGs) over 1994~2011 and anthropogenic aerosol (AA) emissions over 1994~2010 with AA after 2006 from RCP4.5 scenario (Lamarque et al. 2010, 2011)
EP	Early period (EP 1964~1981)	Climatological temperature and salinity tendencies from relaxation run	EP GHGs over 1964~1981 and AA emissions over 1970~1981
PDGA	Present Day (PD 1994~2011) with GHG and AA forcings	Climatological temperature and salinity tendencies from relaxation run	PD GHG and PD AA emissions
PDG	Present Day (PD 1994~2011) with GHG forcing		PD GHG and EP AA emissions
PDA	Present Day (PD 1994~2011) with AA forcing		EP GHG and PD AA emissions

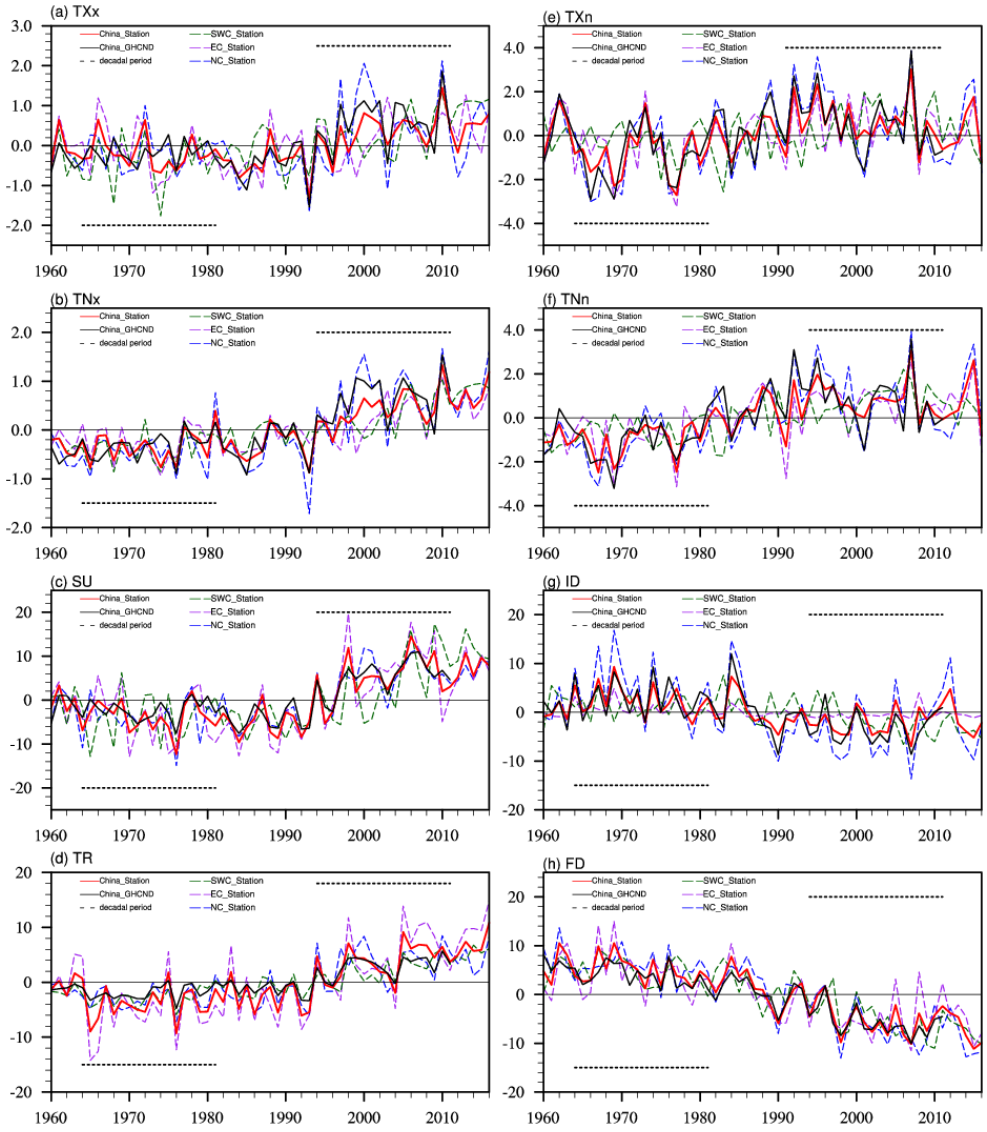

Figure 1. Time series of annual mean temperature extremes anomalies relative to the climatology (mean of the whole period) in summer (TXx, TNx, SU and TR; left panels) and in winter (TXn, TNn, ID and FD; right panels) over China by GHCND dataset (averaged over 20°~55°N, 75°~130°E; black solid lines) and by China station dataset (averaged over 753 stations; red solid lines). The color dashed lines represent the time series of temperature extremes anomalies averaged over three sub-regions by China station dataset (see their distributions in Fig. 2a). Black dashed range bars indicate the early period (EP) of 1964~1981 and the present day (PD) of 1994~2011. Units in TXx, TNx, TXn, and TNn are °C. Units in SU, TR, ID and FD are days.

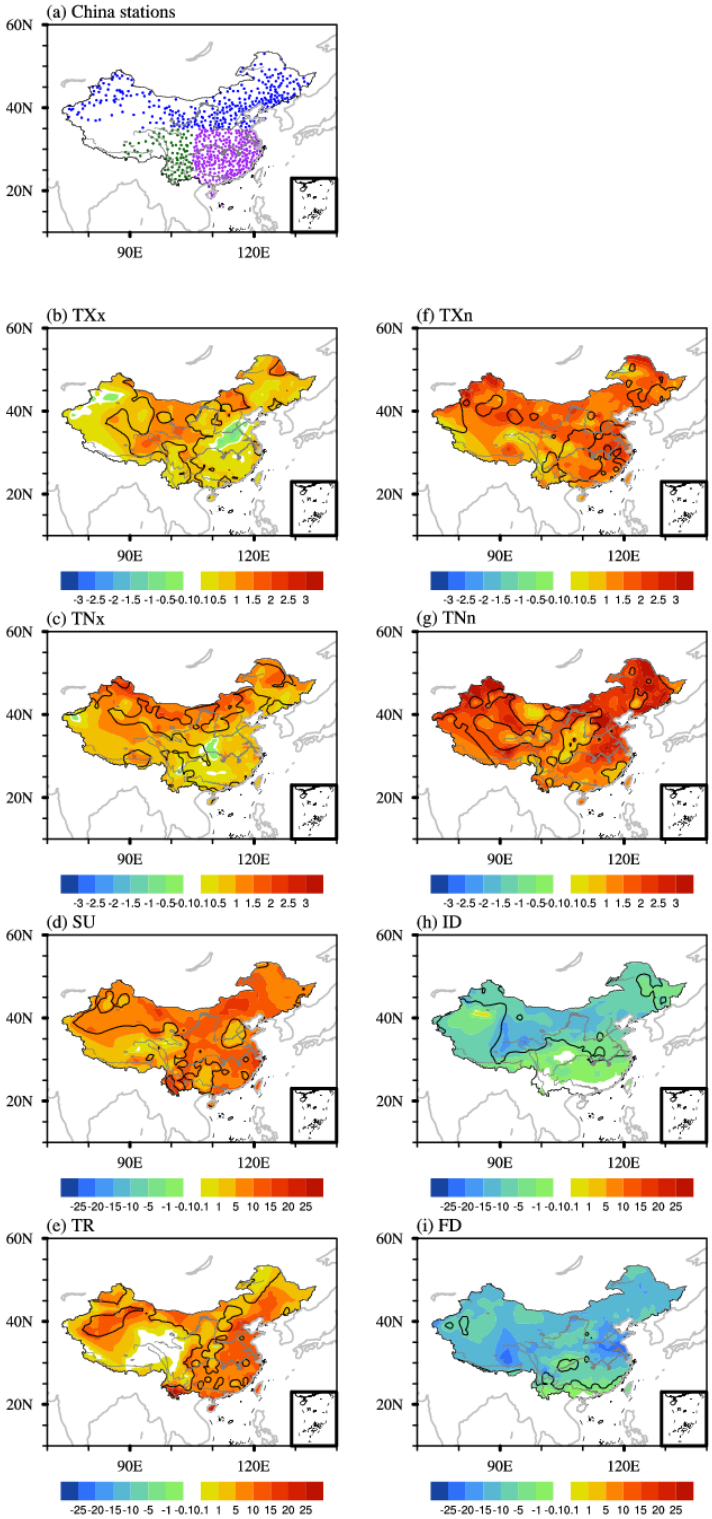

Figure 2. (a) Distributions of 753 stations in China station dataset. The three sub-regional groups are marked with different color dots. The dots in blue, purple and green represent the sub-regions of Northern China (NC), Southeastern China (SEC) and Southwestern China (SWC), respectively. (b)-(i) Spatial patterns of differences in temperature extremes in summer (left panels) and in winter (right panels) between the PD and the EP. The black lines indicate the regions where the changes are statistically significant at the 90% confidence level base on *t*-test. Units in TXx, TNx, TXn and TNn are °C. Units in SU, TR, ID and FD are days.

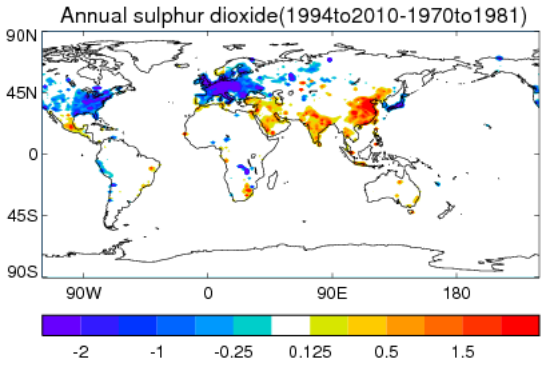

Figure 3. Differences in annual mean sulfur dioxide emissions (units: g m^{-2} yr^{-1}) between 1994~2010 and 1970~1981.

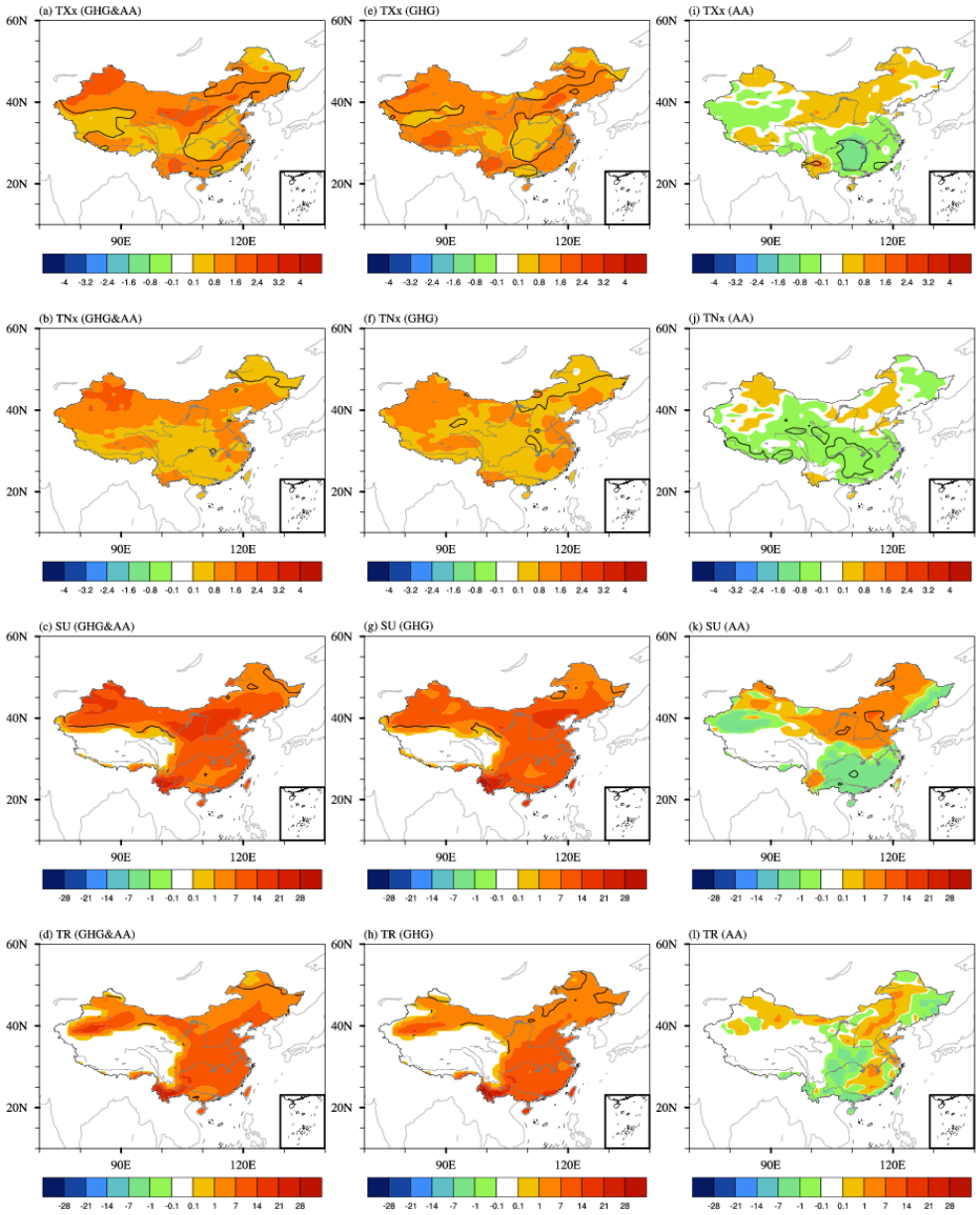

Figure 4. Spatial patterns of changes in hot extremes in response to changes in All forcing (left panels), GHG forcing (middle panels) and AA forcing (right panels), being masked by China boundary. The black lines indicate the regions where the changes are statistically significant at the 90% confidence level base on *t*-test. Units in TXx and TNx are °C. Units in SU and TR are days.

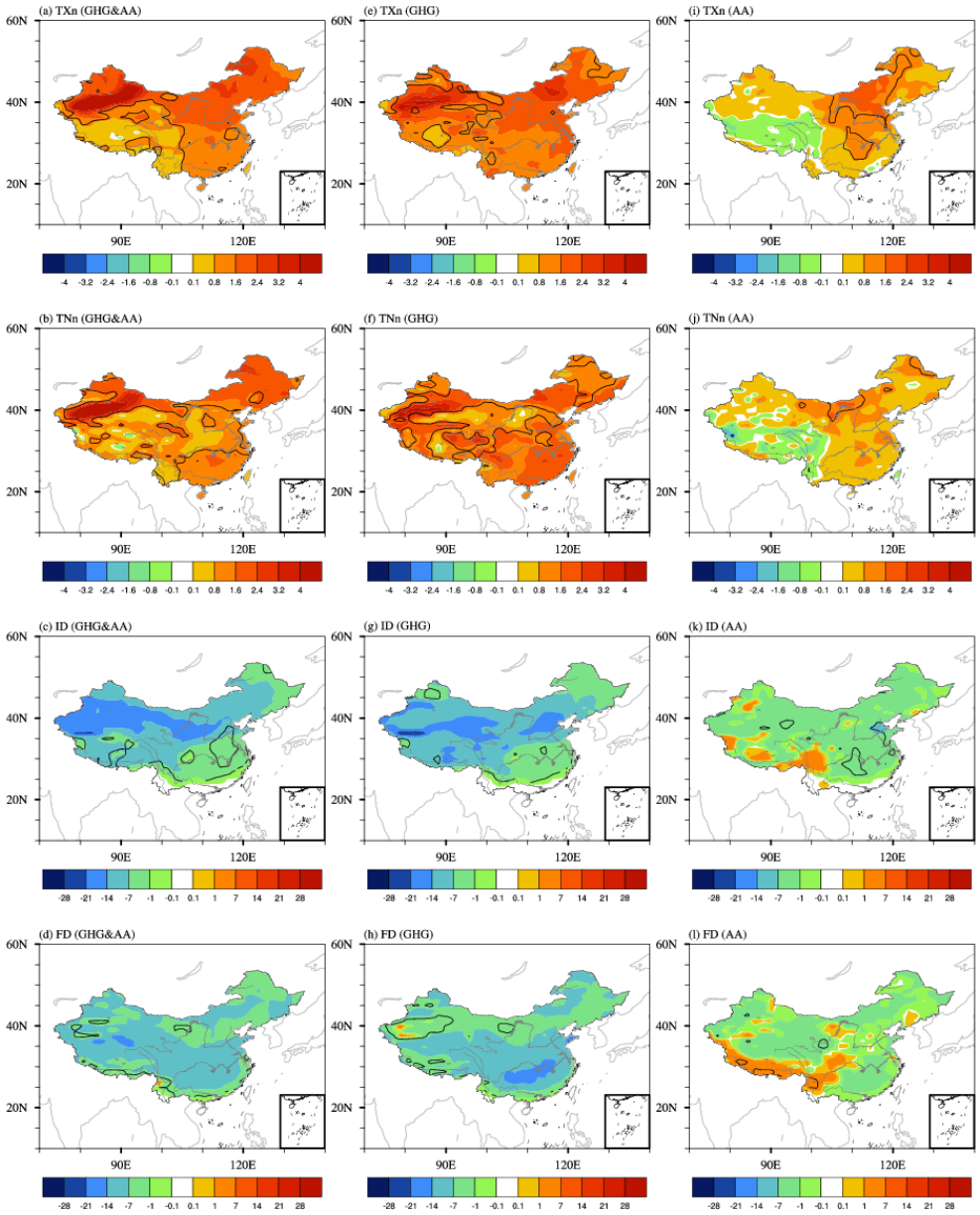

Figure 5. Same as Fig. 4, but for changes in cold extremes. Units in TNx and TNn are °C. Units in ID and FD are days.

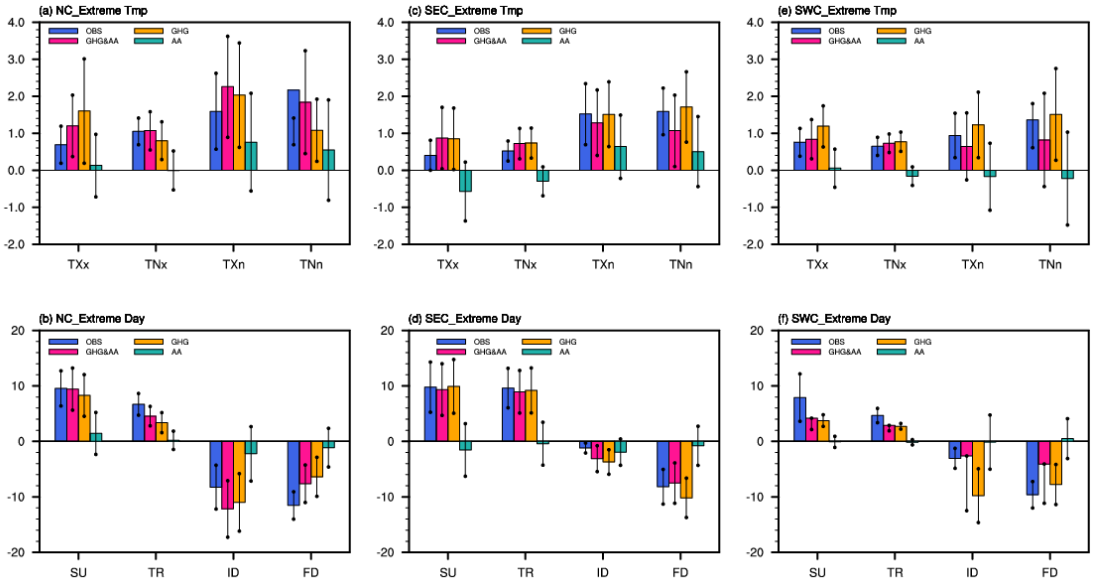

Figure 6. Observed and model simulated changes in temperature extremes in response to different forcings over Northern China (a, b; NC, 35°~55°N, 75°~130°E), Southeastern China (c, d; SEC; 20°~35°N, 105°~130°E) and Southwestern China (e, f; SWC; 20°~35°N, 75°~105°E). The model simulated values have been masked by China boundary. The color bars indicate central estimates and dots show the 90% confidence intervals based on two-tailed Students'*t*-test. Top panels for TXx, TXn, TNx and TNn (units: °C) and bottom panels for SU, TR, ID and FD (units: days).

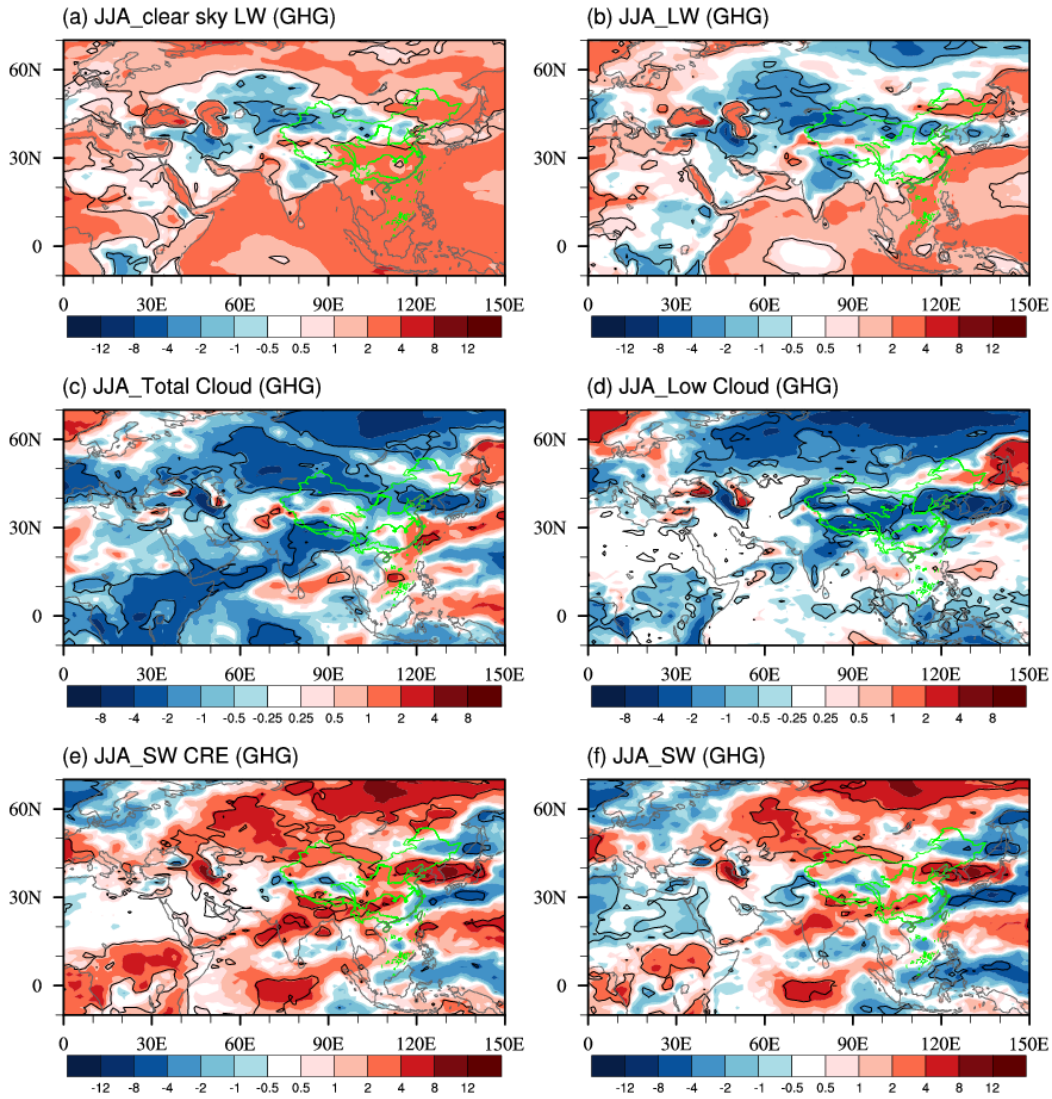

Figure 7. Spatial patterns of summer mean response to changes in GHG forcing: (a) clear sky LW radiation; (b) surface LW radiation; (c) total cloud cover (units: %) (d) low level cloud cover (units: %); (e) SW CRE; and (f) surface SW radiation. Radiation is the net component and in W m^{-2} with positive value meaning downward. The black lines highlight regions where the changes are statistically significant at the 90% confidence level base on *t*-test.

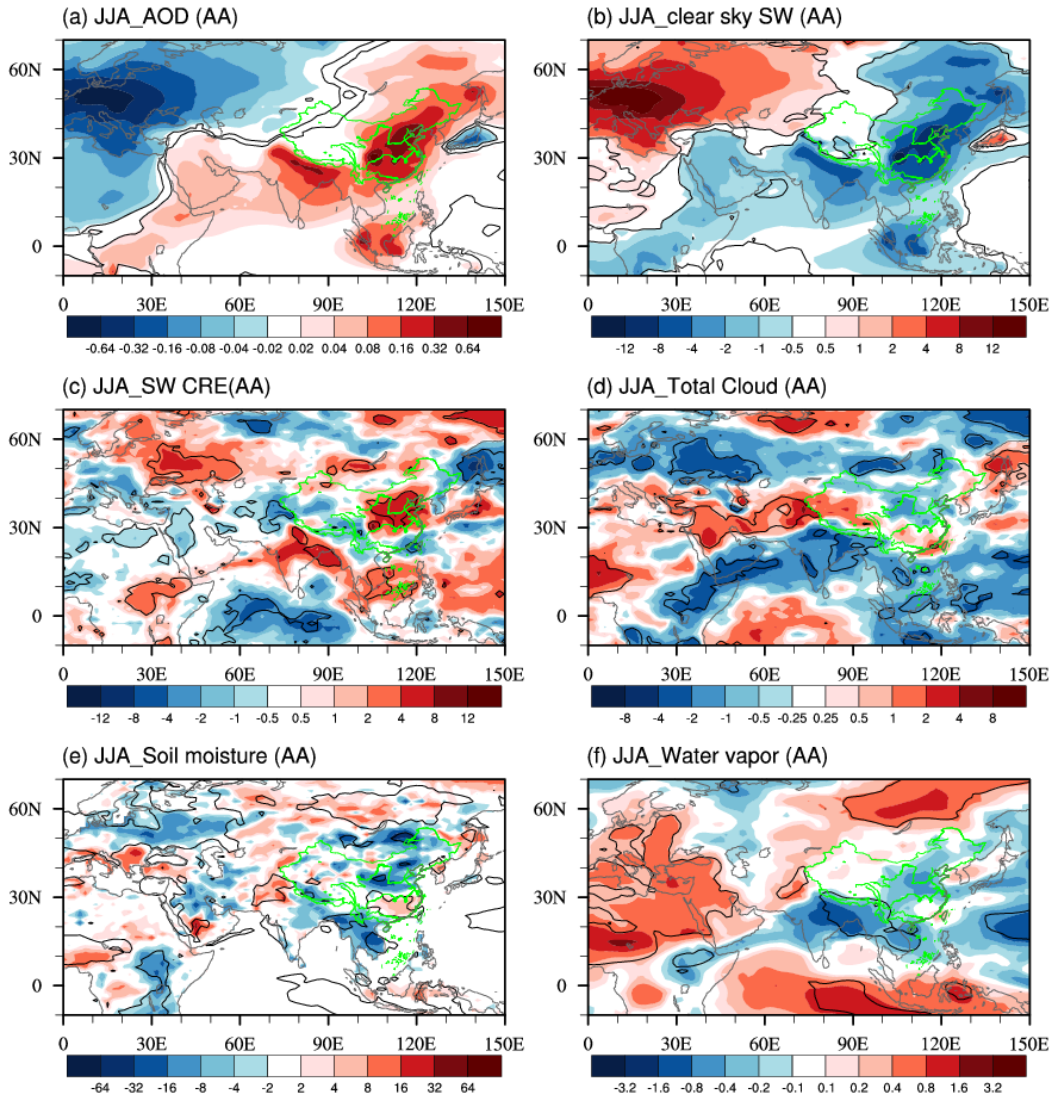

Figure 8. Spatial patterns of summer mean response to changes in AA forcing: (a) total AOD at 0.55 um; (b) clear sky SW radiation; (c) SW CRE; (d) total cloud cover (units: %); (e) soil moisture (units: kg m^{-2}); and (f) column-integrated water vapor (units: kg m^{-2}). Radiation is the net component and in W m^{-2} with positive value meaning downward. The black lines highlight regions where the changes are statistically significant at the 90% confidence level base on *t*-test.

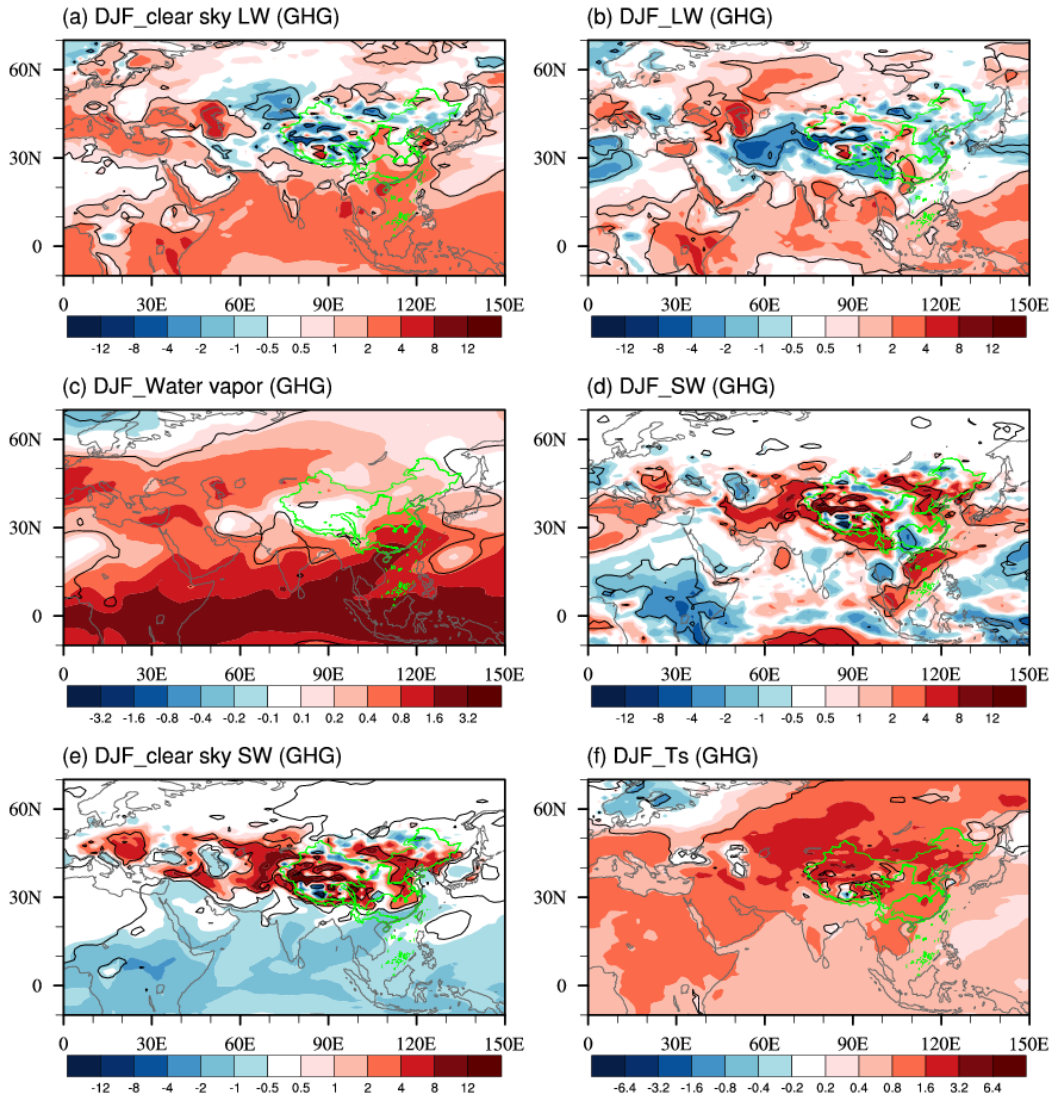

Figure 9. Spatial patterns of winter mean response to changes in GHG forcing: (a) clear sky LW radiation; (b) surface LW radiation; (c) column-integrated water vapor (units: kg m^{-2}); (d) surface SW radiation; (e) clear sky SW radiation; and (f) skin temperature (units: ºC). Radiation is the net component and in W m^{-2} with positive value meaning downward. The black lines highlight regions where the changes are statistically significant at the 90% confidence level base on *t*-test.

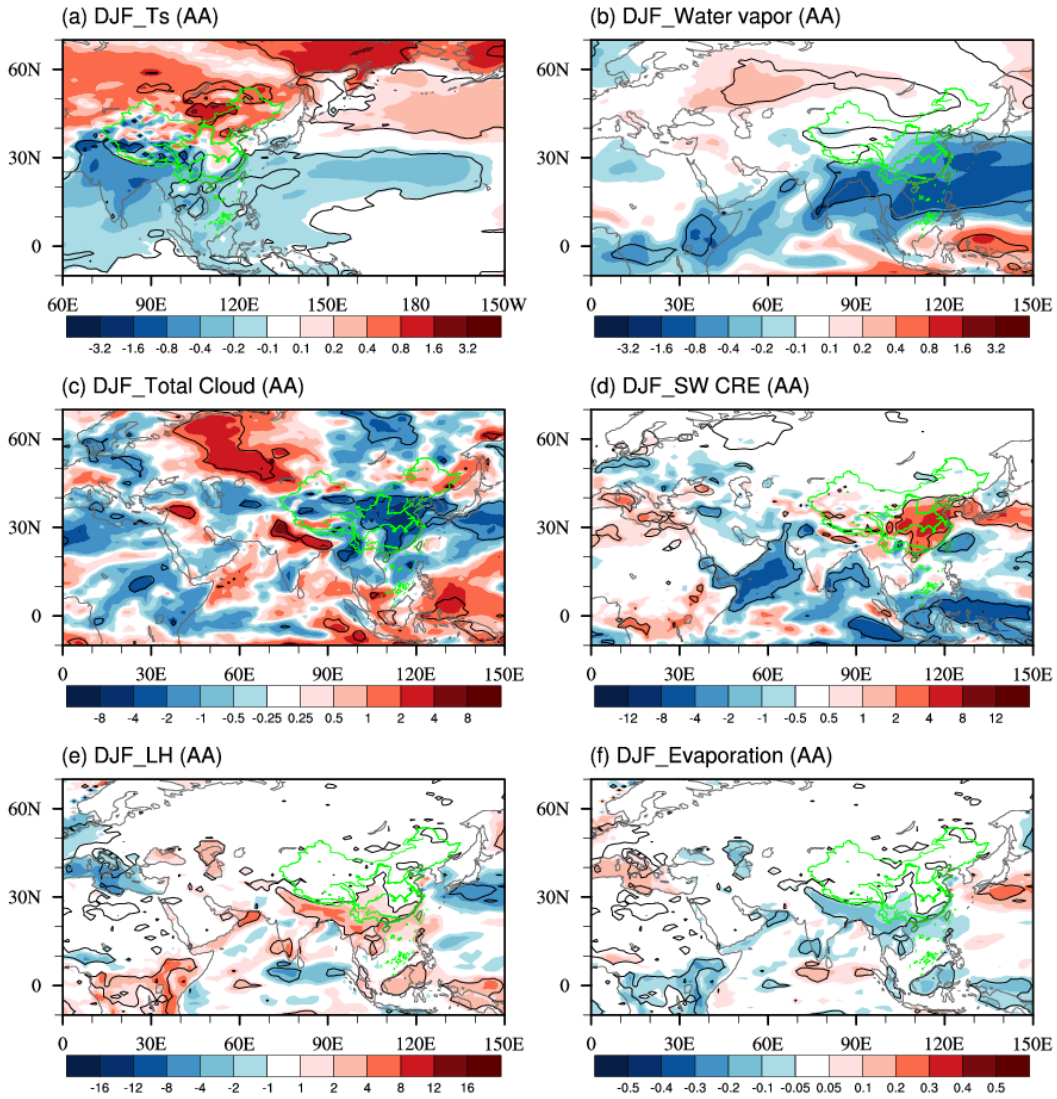

Figure 10. Spatial patterns of winter mean response to changes in AA forcing: (a) skin temperature (units: ºC); (b) column-integrated water vapor (units: kg m^{-2}); (c) total cloud cover (units: %); (d) SW CRE; (e) surface latent hear flux; and (f) evaporation (units: kg m^{-2}). Radiation and flux are in W m^{-2} with positive value meaning downward. The black lines highlight regions where the changes are statistically significant at the 90% confidence level base on *t*-test.